POLITECNICO DI TORINO
Repository ISTITUZIONALE

# Entropy-driven mechanisms in P2-type layered oxide cathodes for sodium-ion batteries: new insights from first-principles and electrochemical analysis

*Original*
Entropy-driven mechanisms in P2-type layered oxide cathodes for sodium-ion batteries: new insights from first-principles and electrochemical analysis / Massaro, A., Porporato, S., Botros, M., Piovano, A., Darjazi, H., Stenzel, D., Meligrana, G., Munoz-Garcia, A.B., Breitung, B., Pavone, M., Gerbaldi, C.. - In: JOURNAL OF MATERIALS CHEMISTRY. A. - ISSN 2050-7488. - 14:30(2026), pp. 19341-19353. [10.1039/d6ta00673f]

*Availability:*
This version is available at: 11583/3011587 since: 2026-06-02T10:31:18Z

*Publisher:*
Royal Society of Chemistry - RSC

*Published*
DOI:10.1039/d6ta00673f

*Terms of use:*

This article is made available under terms and conditions as specified in the corresponding bibliographic description in the repository

*Publisher copyright*

(Article begins on next page)

05 October 2026

Journal of Materials Chemistry A

ROYAL SOCIETY OF CHEMISTRY

PAPER

View Article Online
View Journal | View Issue

Check for updates

Cite this: J. Mater. Chem. A, 2026, 14, 19341

# Entropy-driven mechanisms in P2-type layered oxide cathodes for sodium-ion batteries: new insights from first-principles and electrochemical analysis

Arianna Massaro, *[ab] Silvia Porporato, [bc] Miriam Botros, *[d] Alessandro Piovano, *[bc] Hamideh Darjazi, [bc] David Stenzel, [d] Giuseppina Meligrana,[bc] Ana B. Muñoz-García, [be] Ben Breitung, [d] Michele Pavone [ab] and Claudio Gerbaldi [bc]

P2-type $Na_xMO_2$ layered oxides ($x < 1$) are highly promising cathodes for Na-ion batteries (NIBs) but suffer from phase transitions, transition-metal (TM) migration, and structural distortions that limit cycling stability. Here, we combine first-principles modeling and electrochemical measurements to elucidate how configurational entropy governs their structural and electronic response. By comparing low-, medium-, and high-entropy compositions, we show that higher configurational entropy mitigates TM-centered octahedral distortions, suppresses shear-type deformations associated with P2 → O2 transitions *via* layer gliding, and distributes redox activity across multiple cations (Ni, Co, Fe), avoiding local over-oxidation. Defect-formation analyses reveal that high-entropy mixing significantly discourages out-of-layer TM migration, reducing TM/$Na_{vac}$ antisite formation and stabilizing the layered framework upon deep desodiation. Consistently, medium- and high-entropy materials exhibit superior capacity retention and structural reversibility compared to the low-entropy analogue, with further performance enhancement when using room-temperature ionic-liquid (RTIL)-based NaFSI-$Pyr_{14}$FSI electrolyte, which mitigates Mn dissolution and accounts for enhanced efficiency upon cycling. These findings demonstrate that configurational entropy is a powerful design parameter for achieving robust, high-performance P2-type layered cathodes and provide clear guidelines for entropy-assisted materials engineering in next-generation NIBs.

Received 23rd January 2026
Accepted 7th April 2026

DOI: 10.1039/d6ta00673f

rsc.li/materials-a

Open Access Article. Published on 09 April 2026. Downloaded on 6/2/2026 11:29:15 AM. This article is licensed under a Creative Commons Attribution-NonCommercial 3.0 Unported Licence.

## 1. Introduction

Driven by the demand for sustainable and cost-effective storage technologies, secondary Na-ion batteries (NIBs) have re-emerged as promising alternative to Li-ion batteries (LIBs), particularly in sectors where materials abundance and low cost are essential, such as grid-level/residential stationary energy storage, light mobility, backup power systems, low-cost electronics and Internet of Things (IoT).[1] Owing to the natural abundance and low cost of sodium, NIBs offer a viable pathway toward greener electrochemical technologies.[2] In NIBs, the cathode material is the primary factor dictating the achievable energy density, structural stability, and cycling lifetime, as most degradation mechanisms and voltage-limiting processes originate from the layered cathode framework. As such, its design is central to the development of next-generation Na-based storage systems.

Among the various cathode families, layered transition-metal oxides with the general formula $Na_xTMO_2$ (TM = transition metal) have attracted considerable attention due to their high theoretical capacities and favorable $Na^+$ transport properties.[3] According to the Delmas notation, these materials are categorized into O3, P3, P2, and O2 structures depending on the stacking of the $TMO_2$ layers and the coordination environment of $Na^+$ ions.[4] In particular, P2-type oxides, where $Na^+$ ions reside in trigonal prismatic sites, enable faster diffusion kinetics compared to O3-type counterparts, making them appealing for high-rate applications.[5] However, their structural reversibility remains a challenge: repeated $Na^+$ extraction at high voltages

[a]Department of Chemical Sciences, University of Naples Federico II, Via Cintia 21, Napoli 80126, Italy. E-mail: arianna.massaro@unina.it

[b]National Reference Centre for Electrochemical Energy Storage (GISEL), INSTM, Via Giusti 9, Firenze 50121, Italy. E-mail: alessandro_piovano@polito.it

[c]GAME Lab, Department of Applied Science and Technology (DISAT), Politecnico di Torino, Corso Duca degli Abruzzi 24, Torino 10129, Italy

[d]Institute of Nanotechnology, Karlsruhe Institute of Technology (KIT), Hermann-von-Helmholtz Platz 1, 76344 Eggenstein-Leopoldshafen, Germany. E-mail: miriam.botros@kit.edu

[e]Department of Physics "E. Pancini", University of Naples Federico II, Via Cintia 21, Napoli 80126, Italy

Open Access Article. Published on 09 April 2026. Downloaded on 6/2/2026 11:29:15 AM. This article is licensed under a Creative Commons Attribution-NonCommercial 3.0 Unported Licence.

(>4.2 V) can induce P2 → O2 transitions *via* layer gliding or TM migration, leading to capacity fading and voltage hysteresis.[6,7] Furthermore, Mn-based P2 oxides, though cost-effective and environmentally benign, suffer from Jahn–Teller distortions associated with $Mn^{3+}$ formation at low potentials, causing lattice strain and structural degradation.[8–10] Strategies to mitigate these issues include compositional tailoring, partial TM substitution, and the introduction of structural disorder to enhance robustness and suppress phase transitions.[11–14]

Recently, the high-entropy concept, originally proposed for multicomponent alloys,[15] has emerged as a promising route to design structurally and chemically resilient electrode materials.[16] By incorporating multiple metal species into a single-phase lattice, a large configurational entropy term can stabilize metastable phases, promote homogeneous cation distribution, and trigger beneficial "cocktail effects".[17,18] Both O3- and P2-type high-entropy layered oxides have demonstrated enhanced cycling stability and rate capability compared to their low-entropy analogues.[19,20] Nevertheless, the fundamental mechanisms by which configurational entropy influences structure, electronic behavior, and electrochemical stability remain insufficiently understood.

In this work, we address this knowledge gap by combining first-principles calculations and electrochemical characterization to elucidate the role of configurational entropy in the stabilization of P2-$Na_xMO_2$ cathodes (where M = Mn, Ni, Co, Ti, Mg, Al, Fe). Configurational entropy at the metal site can be easily calculated from the compound's stoichiometry as:

$$S = -R\sum x_i \ln(x_i) \quad (1)$$

Accordingly, compositions are classified as low-, medium-, or high-entropy when the corresponding configurational entropy ($S$) is lower than 1.0$R$, lies in the 1.0–1.5$R$ range, or exceeds 1.5$R$, respectively. Herein, three representative compositions with increasing entropy are investigated as model systems. Through DFT and hybrid-DFT analyses, we examine the local structural distortions, electronic structure evolution, and defect formation tendencies upon Na extraction. These computational insights are directly correlated with experimental evidence from X-ray diffraction (XRD), cyclic voltammetry (CV), and galvanostatic cycling (GC), enabling a comprehensive understanding of how entropy governs the structural and electrochemical responses of P2-type cathodes. Consistently, when experimentally tested in lab-scale Na-based electrochemical cells, medium- and high-entropy oxide materials (hereafter referred to as MEO and HEO) exhibit superior capacity retention and structural reversibility compared to the low-entropy analogue (LEO). Further performance enhancement is attained when cycling the MEO and HEO cathode materials using a room-temperature ionic liquid (RTIL)-based electrolyte (*i.e.*, sodium bis(fluorosulfonyl)imide salt (NaFSI) dissolved in *N*-butyl-*N*-methylpyrrolidinium bis(fluorosulfonyl) imide ($Pyr_{14}FSI$)), suggesting a pivotal role of RTIL solvents in suppressing Mn dissolution and promoting the formation of a denser and more stable solid electrolyte interphase (SEI). Although the reported electrochemical performance does not yet exceed that of state-of-the-art cathodes, this work represents a substantive conceptual advance by delivering new fundamental understanding of entropy-driven stabilization in NIB cathodes, and by articulating clear design principles for next-generation materials. Rather than introducing new compositions, the study reveals previously unexplored mechanistic insights, demonstrating how configurational entropy can be deliberately harnessed to stabilize functional cathode frameworks and guide the rational development of high-performance NIB systems.

## 2. Experimental section

### 2.1. Materials synthesis

The P2-type cathode materials $Na_{0.68}Mn_{0.68}Ni_{0.32}O_2$, $Na_{0.68}Mn_{0.44}Ni_{0.19}Co_{0.25}Ti_{0.09}Mg_{0.03}O_2$, and $Na_{0.68}Mn_{0.44}Ni_{0.19}Co_{0.19}Ti_{0.09}Mg_{0.03}Al_{0.05}Fe_{0.01}O_2$, respectively low-entropy, medium-entropy and high-entropy (namely, LEO, MEO and HEO) were synthesized *via* solid–state reactions. In the first step, stoichiometric amounts of the precursors $Na_2CO_3$ (Acros Organics, 99.95%), MgO (abcr GmbH, 99.5%), $Al_2O_3$ (Alfa Aesar, 99.5%), $TiO_2$ (Alfa Aesar, 99.5%), $Mn_3O_4$ (abcr GmbH, 97%), $Fe_3O_4$ (Alfa Aesar, 97%), $Co_3O_4$ (Alfa Aesar, 99%) and NiO (Alfa Aesar, 99%) were thoroughly mixed by ball milling at 400 rpm for 2 h and compacted into pellets under 5 tons. The pellets were then heated to 500 °C for 2 hours and calcined at 900 °C for 12 hours under air. The final product was obtained by naturally cooling to room temperature and then kept inside an Ar-filled glovebox ($O_2$ < 0.1 ppm, $H_2O$ < 0.1 ppm) to prevent further air exposure.

### 2.2. Computational details and structural models

The series of P2-type layered oxide cathodes, LEO, MEO and HEO, was modeled using three 8 × 4 × 1 supercells of $Na_{0.68}MO_2$ parent material containing 236 atoms within the $P6_3/mmc$ hexagonal space group. Mixed metal occupancy at the 2a Wyckoff site (*i.e.*, the M one) introduces configurational disorder, which was simulated *via* the special quasi-random structure (SQS) approach, as implemented in the *mcsqs* module of the Alloy Theoretic Automated Toolkit (ATAT) package.[21,22] For each material, SQS optimization was performed by matching pair and triplet correlation functions up to a maximum triplet radius of 5.0 Å. The final structures exhibit correlation mismatches below ~0.03 for all targeted clusters, demonstrating a close approximation to a fully random alloy. Na atoms have been placed in edge and face sites with Na(e)/Na(f) ratio being close to 2. To simulate the cathode charge, we model the P2-$Na_xMO_2$ series by varying the sodium content with $x_{Na}$ = 0.68, 0.50, 0.30, 0.12, with desodiation upon charge representing different States of Charge (SoC). Spin-polarized density functional theory (DFT) calculations have been performed with the DFT+$U$ Hubbard-like correction scheme to overcome the large self-interaction error (SIE) that affects DFT when applied to mid-to-late first row TM oxides with unpaired tightly localized electrons in d orbitals. Projector-augmented

 This journal is © The Royal Society of Chemistry 2026

Open Access Article. Published on 09 April 2026. Downloaded on 6/2/2026 11:29:15 AM. This article is licensed under a Creative Commons Attribution-NonCommercial 3.0 Unported Licence.

wave (PAW) potentials and plane wave (PW) basis sets have been used, as implemented in the Vienna *Ab initio* Simulation Package (VASP) code (version 6.4.2).[23–25] For all the calculations, the following PAW potentials have been considered: Na_pv [Be] $2p^6 3s^1$; Mn [Ar]$3d^7$; Ni [Ar]$3d^{10}$; Co [Ar]$3d^9$; Ti [Ar]$3d^4$; Mg [Ne] $3s^2$; Al [Ne]$3s^2 3p^1$; Fe [Ar]$3d^8$; O[He]$2s^2 2p^4$. The Perdew–Burke–Ernzerhof (PBE) exchange–correlation functional has been employed with $U_{eff} = 4.0$ eV parameter for Mn, Ni, Co, and Fe atoms. This choice of a common effective $U$ value has been validated against hybrid DFT in similar systems.[26] The D3-BJ dispersion correction was also added to account for van der Waals (vdW) interactions that play a crucial role in layered structures.[27–29] A kinetic cut-off energy of 600 eV and $\Gamma$-point only sampling have been used; these values ensure converged energies within 3 meV per f.u. with respect to the PW basis set size and Brillouin zone sampling, respectively. For all the self-consistent field calculations, the convergence threshold for total energy has been set to $10^{-5}$ eV. Lattice constants and atomic positions have been fully relaxed until the maximum forces acting on each atom were below 0.03 eV Å$^{-1}$. Single-point calculations have been carried out at the hybrid DFT level of theory with the range-separated Heyd–Scuseria–Ernzerhof density functional with a screening parameter $\mu$ set to 0.2 Å$^{-1}$ (*i.e.*, HSE06), and analysis reported in terms of projected density of states (PDOS) and net magnetization on TM atoms.[30]

### 2.3. Structural and electrochemical characterization

The crystalline structure of the samples was analyzed by X-ray diffraction (XRD), using a Xpert3 MRD Panalytical diffractometer, equipped with Cu Kα radiation source. The XRD patterns were collected in Bragg–Brentano geometry in the $2\theta$ range of 30°–80°. Rietveld refinement was performed with FullProf Suite software.

For electrochemical tests, electrodes were prepared with a composition of 70 wt% of active material, 20 wt% of C-65 (from Imerys) as conductive carbon additive, and 10 wt% polyvinylidene fluoride (PVdF, Solef 5130 from Solvay) as binder. The three components were mixed in dry conditions and then dispersed in *N*-methyl pyrrolidone (NMP, from Sigma-Aldrich), forming a homogeneous slurry (solid content ≈30%) that was then cast onto the Al current collector (from MSE Supplies) using a doctor-blade (indicative thickness of 200 μm of wet film). NMP solvent was removed by evaporation at ambient temperature and further drying under dynamic vacuum at 120 °C for 24 h prior to be transferred into an Ar-filled glovebox (MBraun, $O_2$ and $H_2O$ levels < 1 ppm). The thickness reduces to about 50 μm, with an active mass loading in electrodes of *ca.* 3 mg cm$^{-2}$. Na-metal cells were assembled within ECC-Std test cells (EL-Cell GmbH), using metallic Na (from Sigma-Aldrich) as counter electrode, a Whatman GF/A glass wool disk as the separator, and as electrolyte either $NaClO_4$ 1 M in propylene carbonate (from Solvionic) or NaFSI in $Pyr_{14}FSI$ (molar ratio of 1 : 4, from Solvionic). Cyclic voltammetry (CV) was performed on a VMP3 workstation (Bio-Logic Instruments) using Swagelok-type 3-electrode cells in the range from 1.9 to 4.2 V *vs.* $Na^+$/Na with a scan rate of 0.1 mV s$^{-1}$. Galvanostatic cycling tests were carried out at ambient laboratory temperature (≈25 °C) with an ARBIN BT2000 battery tester, from 2.0 to 4.2 V *vs.* $Na^+$/Na, setting the current densities on the basis of an expected capacity of 100 mAh g$^{-1}$. For both CV and galvanostatic cycling test the cut-off voltage was set to 4.2 V *vs.* $Na^+$/Na to avoid any irreversible phase transitions, as already reported in previous studies for analogous materials at very high voltages.[31] In this way, we could compare the redox behavior of the three materials under the same sodiation/desodiation conditions; as a matter of fact, the behavior of the three materials is expected to greatly diverge at high voltages, as shown in the sodiation/voltage profile computed with DFT (see Fig. S2 in SI)). The reproducibility of the electrochemical measurements was verified by testing additional cells under identical conditions. Therefore, representative results are reported in the manuscript.

## 3. Results and discussion

The key properties of LEO, MEO and HEO are hereby addressed in terms of their physicochemical and electrochemical characteristics, with the primary aim of elucidating the role of configurational entropy in determining their stability, performance, and potentiality for future applications in NIBs.

In the following, we provide an in-depth analysis on the structural and electronic features of LEO, MEO and HEO, as well as their evolution upon charging, as revealed by first-principles calculations. Furthermore, we assess their electrochemical performance in laboratory-scale NIB cells employing both standard electrolytes based on organic solvents ($NaClO_4$ 1M in PC) and RTIL-based electrolytes (NaFSI in $Pyr_{14}FSI$ 1 : 4). Our goal is to emphasize the influence of mixing entropy on the structural stability of layered oxide cathodes, and to showcase promising implementations using innovative electrolytes for high-performance energy storage devices.

Fig. 1a displays the XRD patterns of the three as-synthesized samples, the diffraction peaks of which are all assigned as reflections of $P6_3/mmc$ hexagonal space group.[32,33] The results of Rietveld refinement (perfectly aligned with previous works on these materials)[16] are reported in Fig. S1 and Table S1, pointing out a slight shrinkage of the cell volume with increasing entropy (from 80.8 to 79.9 Å$^3$ for LEO and HEO, respectively). The first-principles characterization shows a good agreement with XRD data, the lattice constants being optimized at PBE+*U*-D3BJ level of theory within <1% error deviation from experiments (as shown in Fig. 1b). To account for mixing entropy and to reliably model homogeneously distributed arrangements, the Na/vacancy and metal atoms orderings are incorporated into the crystalline lattice using the SQSgen code, which leads to the geometry solution corresponding to the maximum configurational entropy (*i.e.*, special quasi-random structures, SQS).[34] The SQS results for the three systems within the $MO_2$-layers can be visualized in Fig. 1c.

### 3.1. Charge compensation mechanisms regulated by configurational entropy

Once the model structure was established, theoretical investigation has been carried out to address the electrochemical behavior of the explored cathodes, namely the evolution of their

Open Access Article. Published on 09 April 2026. Downloaded on 6/2/2026 11:29:15 AM.
This article is licensed under a Creative Commons Attribution-NonCommercial 3.0 Unported Licence.

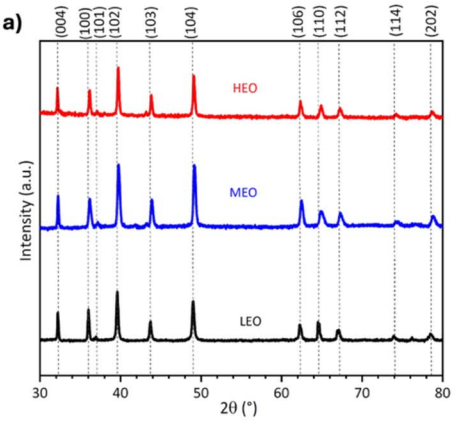


b)

| | a,b (Å) | | c (Å) | |
|---|---|---|---|---|
| | *exp.* | *theo.* * | *exp.* | *theo.* |
| **LEO** | 2.8912 | 2.909 (0.6%) | 11.1641 | 11.233 (0.6%) |
| **MEO** | 2.8742 | 2.887 (0.5%) | 11.1385 | 11.155 (0.2%) |
| **HEO** | 2.8757 | 2.891 (0.5%) | 11.1532 | 11.169 (0.2%) |

** theoretical values are rescaled with respect to the unit cell.*

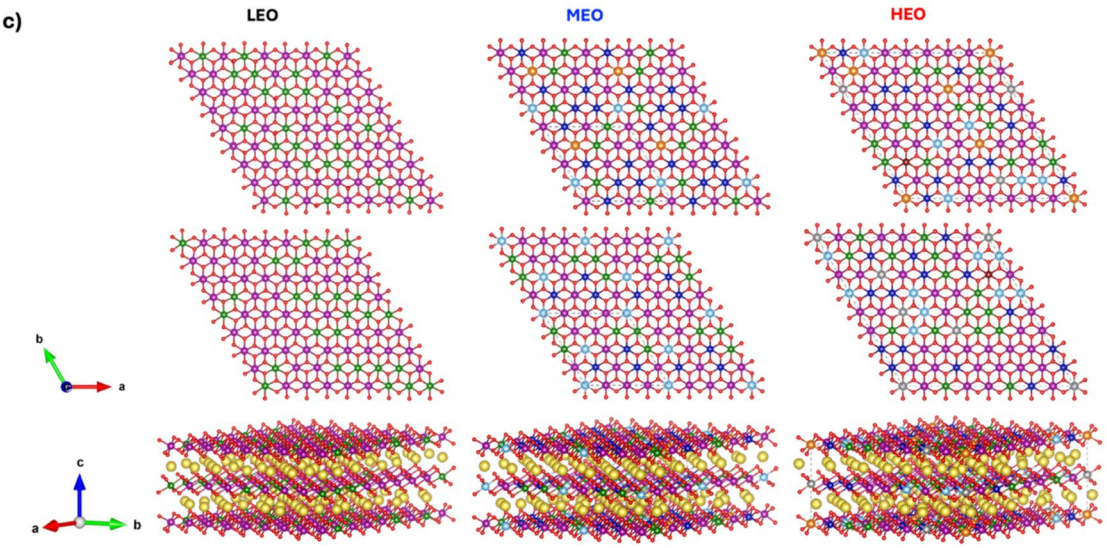


Fig. 1 (a) XRD diffractograms of the three P2-$Na_xMO_2$ samples, labelled as LEO, MEO and HEO, with the reflections indexed according to $P6_3/mmc$ hexagonal space group. (b) Lattice parameters of the three samples as obtained from Rietveld refinement and PBE+*U*-D3BJ level of theory. Percentage error deviation is reported in parentheses. (c) Structural theoretical models for P2-$Na_xMO_2$ compounds: (top) random distribution of metal atoms within the $MO_2$-layers; (bottom) 3D view of the hexagonal cells in the $P6_3/mmc$ space group. Atoms are represented as spheres. Colour code: Na, yellow; Mn, violet; Ni, green; Co, blue; Ti, cyan; Mg, orange; Al, grey; Fe, brown; O, red.

electronic structure at decreasing sodiation, mimicking the charge/discharge process (the voltage/sodiation correlation is shown in Fig. S2, whereas Table S2 reports the corresponding lattice parameters). By analyzing the magnetization trend, we could derive the oxidation states of each transition metal at different sodium contents, thus assigning the involved redox couples at each voltage step. It is noteworthy that such compositionally diverse oxides containing multiple metal atoms with intricate and non-trivial spin configurations call for a proper treatment of the strongly localized d-electrons. Accordingly, we have performed hybrid DFT calculations with the HSE06 functional, which ensures a reliable description of the spin states across all the investigated systems (see PDOS in Fig. S3 of SI). As reported in Fig. 2, Mn is predominantly found in mixed $Mn^{3+}/Mn^{4+}$ oxidation states across all systems, becoming fully oxidized to $Mn^{4+}$ at $x_{Na} = 0.30$. The few $Mn^{3+}$ at high sodium content could act as Jahn–Teller (JT) active centers, and thus may be responsible for structural distortion upon cycling. This aspect will be further highlighted in the following discussion (see Section 3.3). On average, however, Mn oxidation can be considered a minor contribution in all systems (see Fig. S4 in SI). In contrast, Ni exhibits a clear and progressive oxidation from $Ni^{2+}$ to $Ni^{3+}$, and further to $Ni^{4+}$ in MEO and HEO compositions at the highest degree of desodiation. Again, the presence of JT-active $Ni^{3+}$ species can result in substantial octahedral distortions, as clarified below. Similarly, Co undergoes sequential oxidation from $Co^{3+}$ to $Co^{4+}$ in both MEO and HEO at $x_{Na} = 0.30$. Finally, in HEO, Fe also participates in the redox process through a $Fe^{3+} \rightarrow Fe^{4+}$ oxidation upon sodium removal. Overall, these results demonstrate that Ni, Co and Fe are the primary redox active species responsible for charge compensation during desodiation. Because multiple species share the redox burden, the systems avoid local over-oxidation and evenly distribute not only structural but also electronic changes. This facilitates redox processes and enables more stable electrochemical response of higher-entropy compounds (MEO and HEO) compared to LEO.

 This journal is © The Royal Society of Chemistry 2026

Open Access Article. Published on 09 April 2026. Downloaded on 6/2/2026 11:29:15 AM.
This article is licensed under a Creative Commons Attribution-NonCommercial 3.0 Unported Licence.

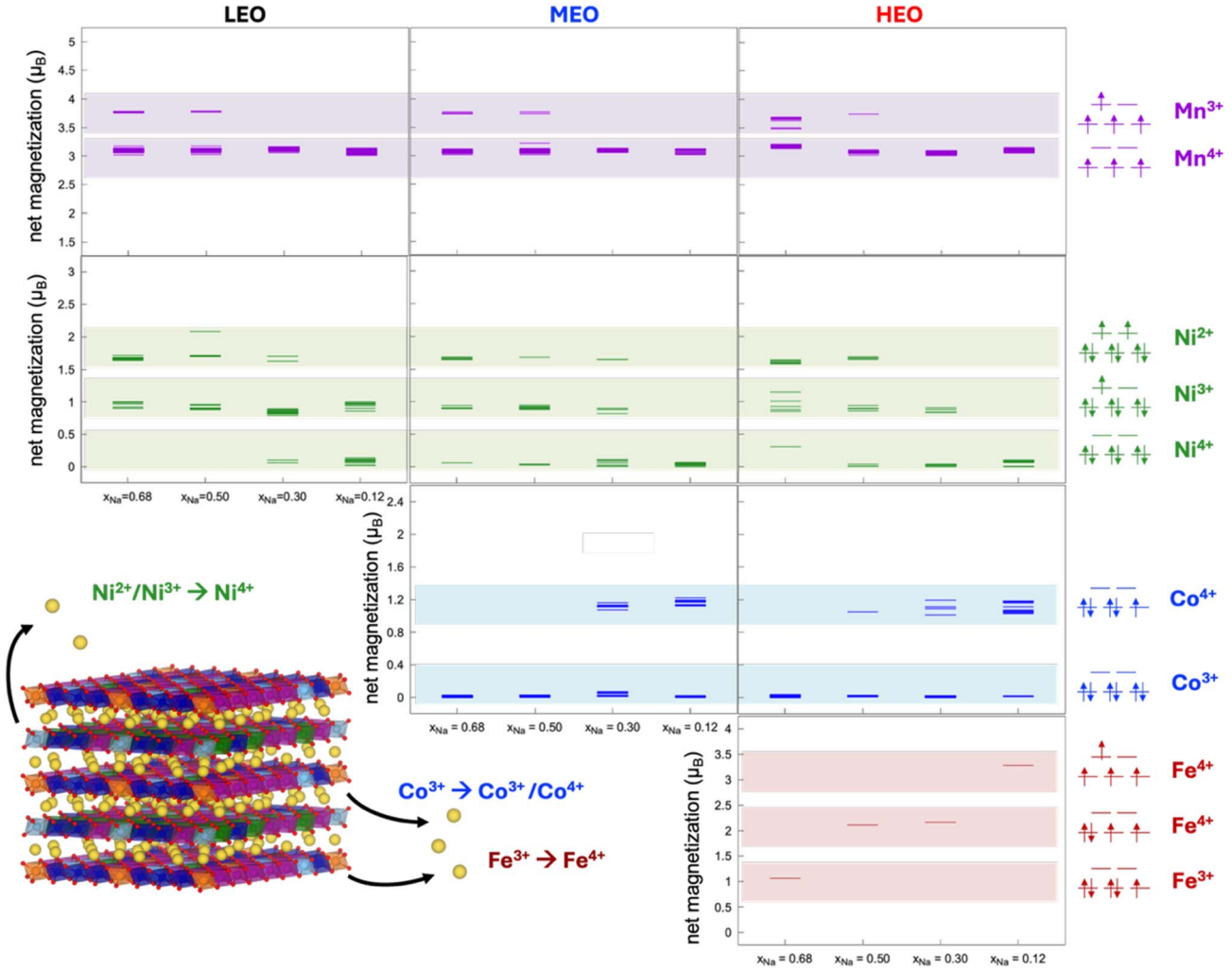


Fig. 2 Electronic structure analysis: net magnetization of Mn, Ni, Co and Fe atoms in LEO, MEO and HEO as function of sodiation degree computed at HSE06 level of theory. Electronic configurations are declared. Inset: pictorial representation of a P2-$Na_xMO_2$ lattice with the redox couples involved in the charge compensation upon $Na^+$ extraction. Color code as in Fig. 1, Na yellow. Polyhedral visualization is adopted for the $MO_6$ units.

The theoretical prediction of the redox active species responsible for charge compensation upon desodiation in the three materials is well aligned with the CV profiles experimentally measured in Na-based cells employing a standard electrolyte (*e.g.*, $NaClO_4$ 1M in PC). As visible in Fig. 3 (panels a, b and c), all samples exhibit a first oxidation peak (at 2.0 V *vs.* $Na^+/Na$ for LEO, and at 2.2 V for MEO and HEO) corresponding to the partial conversion of $Mn^{3+}$ to $Mn^{4+}$,[35] which is consistent with the detection of $Mn^{4+}$ species from DFT calculations even at high Na content ($x_{Na} = 0.68$ corresponds to *ca.* 2.5 V *vs.* $Na^+/Na$ according to the capacity–voltage profiles in Fig. S2).

At higher potentials (*i.e.*, increasing desodiation degree), the CV profile of LEO remarkably differs from the other two (Fig. 3a *vs.* 3b and 3c): the $Ni^{2+}/Ni^{3+}$ transition at 3.0 V is barely visible,[36] whereas the rest of the profile is dominated by very intense and sharp peaks due to reversible yet significant structural changes. As reported by Islam *et al.*, *in situ* synchrotron XRD analysis on analogous materials revealed progressive phase transitions from P2 ($P6_3/mmc$) to P′2 ($Cmcm$) and finally to OP4 ($P6_3$) taking place in this voltage range,[35] which were classified by Yan *et al.* as $Na^+$ ions/vacancies ordering processes.[37] On the other hand, the CV profiles of MEO and HEO (Fig. 3b and c, respectively) suggest a more extended redox participation, due to the presence of many redox active species, partially overlapping with each other in the voltage range from 3 to 4 V *vs.* $Na^+/Na$. In particular, both samples display a sharp oxidation peak at 3.0 V due to $Ni^{2+}/Ni^{3+}$ transition,[36] which is followed in the case of MEO by a broad oxidation signal centered at 3.25 V, compatible with $Co^{3+}/Co^{4+}$ transition;[38] such signal is possibly present also in HEO profile, but in that case it is overlapping with a prominent oxidation peak at 3.35 V assigned to $Fe^{3+}/Fe^{4+}$ transition.[36] All these transitions are in fair agreement with the predicted oxidation from the computational results reported in Fig. 2, taking into account the correlation between sodiation degree and voltage shown in Fig. S2. The CV profiles of MEO and HEO also exhibit an oxidation peak at 3.6 V that is reasonably

Open Access Article. Published on 09 April 2026. Downloaded on 6/2/2026 11:29:15 AM.
This article is licensed under a Creative Commons Attribution-NonCommercial 3.0 Unported Licence.

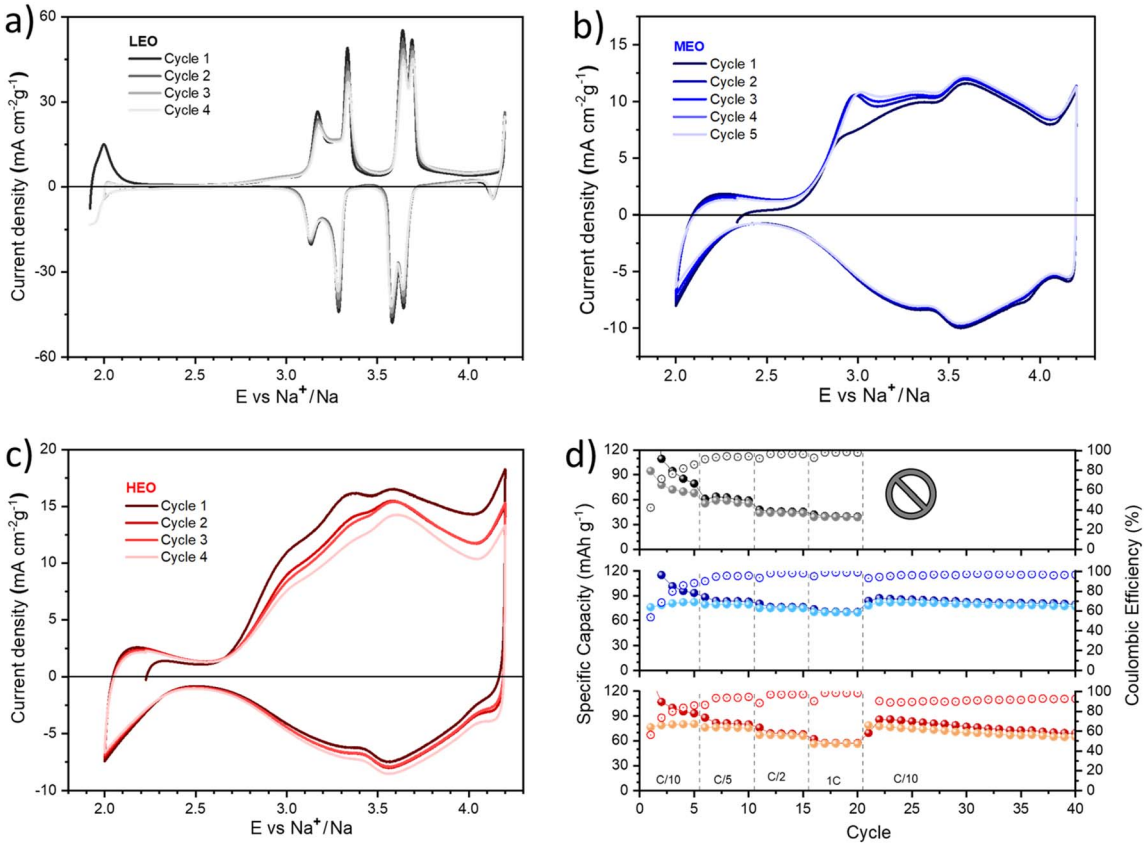


Fig. 3 Cyclic voltammetry curves of (a) LEO, (b) MEO, and (c) HEO with standard electrolyte ($NaClO_4$ 1M in PC). (d) Specific capacity and coulombic efficiency of Na-metal cells based on LEO, MEO, and HEO with standard electrolyte, upon galvanostatic cycling at different C-rates (representative voltage profiles *vs.* specific capacity are reported for each sample in Fig. S5).

associated to $Na^+$ ions/vacancies ordering,[37] and both profiles conclude at 4.2 V with an oxidative current that corresponds to the incipient $Ni^{3+}/Ni^{4+}$ transition; as a matter of fact, DFT results reveal the presence of $Ni^{4+}$ at $x_{Na} = 0.30$, but the whole oxidation peak cannot be properly observed in the profiles of Fig. 3b and c as it closely lies at the cut-off voltage of the CV measurements.[36]

Beyond metal-specific contributions to charge compensation, configurational entropy itself clearly modulates the electrochemical response. Indeed, the CV profiles of LEO and MEO/HEO differ not only in the presence of multiple redox peaks associated with different transition metals, but also in the shape of structure-related signals attributed to Na/vacancy ordering. This indicates that mixing entropy can indirectly tune structural stabilization and evolution during cycling, as examined in detail in the following sections.

### 3.2. Electrochemical performance controlled by configurational entropy

When testing P2-$Na_xMO_2$ samples for galvanostatic charge/discharge cycling in combination with standard liquid electrolyte ($NaClO_4$ 1M in PC), it is well evident that the cell with LEO fails after 20 cycles (top panel in Fig. 3d): after the rate capability test, upon resetting the current to C/10 regime, the cell gets stuck in charging mode without reaching the targeted voltage because all the electric current is consumed in parasitic reactions, such as Mn dissolution. Indeed, even if not expressly quantified in this work, this is a well-known issue of Mn-containing cathodes for NIBs, typically exacerbated at higher SoC.[39] On the other hand, MEO and HEO (middle and bottom panels in Fig. 3d, respectively) demonstrate to completely recover the initial capacity (*ca.* 80 mAh $g^{-1}$) after the rate capability test and stably sustain charge/discharge cycles up to the end of the testing protocol (although with a rather limited coulombic efficiency (CE), *viz.* 97 and 93% for MEO and HEO, respectively). However, also MEO and HEO, tested in these conditions, suffer from high initial polarization, resulting in a CE lower than 90% during the first 6 cycles.

Clearly, managing large compositional diversity arising from metal mixing introduces complexity into the system, which can make any prediction or understanding of electrochemical behavior more difficult. Notwithstanding the beneficial effects that high entropy can induce by delocalizing the electronic response, individual metal species may also promote undesired processes.[40] In principle, a metal ion can migrate into the sodium layer and occupy a vacant Na site, either created during cycling or intrinsically present in Na-deficient formulations.[41] The resulting metal-$Na_{vac}$ antisite defect disrupts the ideal alternating Na-layer/M-layer stacking, leading to partially mixed

 This journal is © The Royal Society of Chemistry 2026

Open Access Article. Published on 09 April 2026. Downloaded on 6/2/2026 11:29:15 AM. This article is licensed under a Creative Commons Attribution-NonCommercial 3.0 Unported Licence.

cation layers.[42] Such defects can be detrimental for the battery performance by causing capacity loss, voltage hysteresis and structural degradation: (i) when sitting in Na sites, the metal ion physically blocks the diffusion channels and lowers the ionic conductivity; (ii) M-rich local environments along $Na^+$ pathways can hinder subsequent $Na^+$ re-insertion, leading to irreversible capacity loss and voltage hysteresis; (iii) metal ion migration can also trigger layer gliding (*e.g.*, P-to-O transitions) and generate local strain that promote structural transformations, micro-cracking and long-term instability; (iv) migrated metal ions can diffuse themselves into the electrolyte and promote detrimental ion dissolution. For all these reasons, the tendency of a P2-$Na_xMO_2$ cathode to release metals from their layers can be considered as an early step toward degradation processes. To clarify this aspect, we focus on the metal ion out-of-layer migration in our investigated P2-$Na_xMO_2$ cathodes, so as to unveil whether the increasing entropy may prevent it, thus inducing major stability toward degradation.

The migration of a metal ion into a sodium vacant site is simulated as the formation of a metal/$Na_{vac}$ antisite defect under deep desodiation conditions ($x_{Na} = 0.30$ and 0.12). We focus on Mn and Ni as the most abundant metals in MEO and HEO formulations and the only species present in LEO. Fig. 4 depicts the energy landscape associated to the process: the overall energetics of antisite formation becomes more favorable at lower sodium content ($\Delta E \sim -0.7$ to 4.6 eV *vs.* $-5.3$ to 1.6 eV at $x_{Na} = 0.30$ and 0.12, respectively), reflecting the stronger interactions established to compensate for the increased number of $Na^+$ vacancies. We should point out that not only negative values of $\Delta E$, but also slightly positive energy variations would still be accessible under the battery operating conditions (*i.e.*, under an applied voltage upon charge), indicating that most of these defects are likely to occur. Across the series, LEO easily accommodates the antisite defects, with the Mn being particularly stabilized at $x_{Na} = 0.12$ due to a 4-fold coordination with the oxygen atom exposed from the opposite $MO_2$-layer. A similar stabilization occurs for the Mn antisite defect in MEO already at $x_{Na} = 0.30$, which is even more pronounced in the 5-fold coordination attained at $x_{Na} = 0.12$. Together with the low-energy Ni antisite defects, MEO clearly allows easy metal out-of-layer migrations, which raises concerns regarding its electrochemical durability. However, the Ni antisite detected at $x_{Na} = 0.12$ retains its $Ni^{4+}$ oxidation state, suggesting that the foreseen capacity loss may remain limited. Conversely, the HEO composition offers a noticeably different behavior, with $\Delta E$ values shifted upward compared to LEO and MEO. At $x_{Na} = 0.30$, Mn antisite formation is highly unfavorable, whereas Ni antisites remain energetically accessible. Further desodiation leads to a mostly unchanged picture for Ni antisite, while Mn antisite formation is slightly stabilized owing to a 5-fold coordinated intermediate. To sum up, the low-entropy composition seems highly prone to out-of-layer metal migration, with thermodynamically convenient formation of $Mn^{2+}/Na_{vac}$ antisite occurring already at $x_{Na} = 0.30$. This finding can be fairly regarded as an easy tendency of LEO to undergo Mn dissolution upon cycling, which could be a feasible reason for the cell failure denoted in Fig. 3d. Even though the energetics of $Mn^{2+}/Na_{vac}$ antisites in MEO seems to suggest accessible intermediates at $x_{Na} = 0.30$, the established geometries in this case are sensibly different. The higher coordination attained by the migrated $Mn^{2+}$ allows to pin the oxide slabs, reinforce the crystalline structure and thus prevent layers gliding, which is the main driver in the P-to-O phase transition. By enabling the formation of migrated yet peculiar $Mn^{2+}$ sites that act as lattice pillars, the medium-entropy composition seems able to limit structure collapse, as confirmed by the stable capacity showed upon cycling (Fig. 3d). Analogously, the steady performance of HEO perfectly aligns with the largely unlikely formation of $Mn^{2+}/Na_{vac}$ at the same SoC predicted by DFT, suggesting a mitigated tendency for Mn dissolution and a consequent enhancement of the electrochemical durability with increasing configurational entropy in the cathode formulation. It is worth mentioning that in the antisite defect calculations, the oxidation state of the transition metal was not imposed *a priori*; instead, the electronic structure was determined self-consistently within the DFT framework, allowing the metal charge state associated with migration into a Na vacancy to emerge naturally from the calculation.

Here, the indirect influence of configurational entropy becomes even more pronounced: despite involving the same

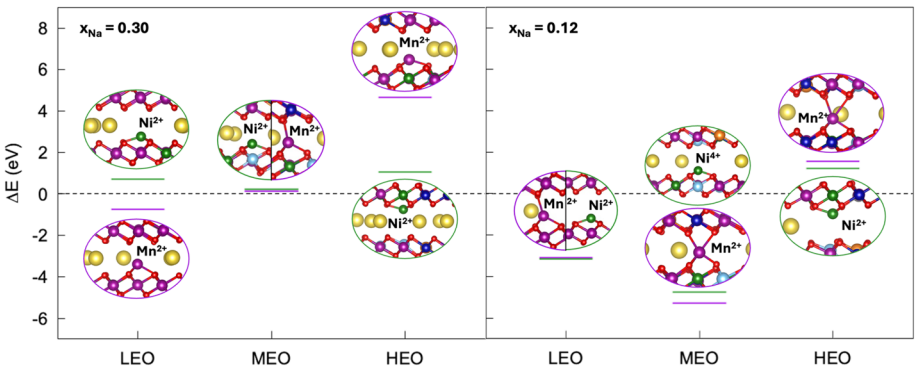


Fig. 4 Mn and Ni out-of-layer migration, *i.e.*, M/$Na_{vac}$ antisite defects. $\Delta E$ is the formation energy of each defect, calculated as the energy difference between the defective and the pristine structure, plotted for LEO, MEO and HEO at (left) $x_{Na} = 0.30$ and (right) $x_{Na} = 0.12$. Insets: structural detail of the optimized configurations. Oxidation states of migrated Mn/Ni are declared. Color code as in Fig. 1.

Open Access Article. Published on 09 April 2026. Downloaded on 6/2/2026 11:29:15 AM. This article is licensed under a Creative Commons Attribution-NonCommercial 3.0 Unported Licence.

metals (Mn and Ni), the three compositions exhibit markedly different behaviors due to their highly diverse local chemical environments. Out-of-layer migration of Mn and Ni into Na vacancies is strongly modulated by configurational entropy, with increasing metal mixing progressively disfavoring the formation of TM/$Na_{vac}$ antisite defects. This highlights the role of entropy in promoting structural robustness by suppressing detrimental cation migrations, which can lead to Mn dissolution and cathode degradation.

### 3.3. Structural effects of configurational entropy

With the scenario depicted so far, we aim at further elucidating the electrochemical performance, stability and durability of our cathode systems. The use of RTIL-based electrolytes is known to beneficially mitigate the detrimental Mn dissolution,[43] by avoiding the formation of the convenient solvation shell around $Mn^{2+}$ that in the case of carbonate solvents can compete with and even exceed the solvation of $Na^+$ ions.[44] Therefore, we employ NaFSI in $Pyr_{14}FSI$ (1 : 4) as electrolyte in combination with the three cathode materials and perform additional galvanostatic cycling tests. The performance of LEO under these conditions considerably improves, with an almost stable capacity of 90 mAh $g^{-1}$ in the first 5 cycles at C/10 (with a CE of 97%) and a good capacity retention after the rate capability test (around 70 mAh $g^{-1}$). The capacity strongly reduces at higher currents (60, 28, and barely 8 mAh $g^{-1}$ at C/5, C/2, and 1C, respectively). Also, in the case of the RTIL-based electrolyte, much better performances are achieved by MEO and HEO (Fig. 5b and c, respectively). HEO, in particular, displays an initial capacity of 83 mAh $g^{-1}$ at C/10 with a CE above 99% starting from the fourth cycle. However, a decrease of the capacity is observed upon increasing current (64, 52 and 42 mAh $g^{-1}$ at C/5, C/2 and 1C, respectively), a decrease even more pronounced than in the case of standard electrolyte (Fig. 3c) reasonably due to the higher viscosity of RTILs compared to carbonates. HEO completely retains the initial capacity upon resetting the current regime to C/10, maintaining a stable performance in terms of capacity and CE (>99%) up to the end of the cycling test (final capacity at the 40th cycle of 76 mAh $g^{-1}$).

The different response of the three materials in the galvanostatic cycling test is reflected also in the *post-mortem* XRD patterns, collected by disassembling the cells in the glovebox after 40 charge/discharge cycles. The XRD pattern of HEO (Fig. 5f) is perfectly maintained, demonstrating the high structural stability of the material that reversibly sustains $Na^+$ insertion/extraction. In the pattern of MEO (Fig. 5e), barely noticeable shifts of some peaks reveal minor changes in the lattice parameters; in particular, the left-shifted peaks related to lattice parameter *c* (such as (004) and (106)) and the right-shifted peaks related to a and b parameters (such as (100), (110) and (112)) indicate a minimal anisotropic cell distortion, with *c*-axis elongation and basal-plane contraction. On the contrary, the pattern of LEO (Fig. 5d) reveals a general decrease in the crystallinity of the material and the coexistence of multiple phases (as previously discussed for the redox processes observed in CV profile in Fig. 3a); for instance, the OP4 phase is well evident with (004) reflection at 31.5°.[45]

Overall, these results confirm the beneficial effect of RTILs as electrolyte solvents with the investigated cathode materials in Na-based cells, especially at low current densities, where longer time usually allows the parasitic reactions to become more relevant and even compete with the main operating redox processes (at high currents this issue is negligible because of the very high rate of the main processes). With CE normally decreasing as current density decreases, the improved performance under low current regime clearly indicates a key role of the RTIL-based electrolyte: the highly electrochemically stable and non-volatile RTIL-based electrolyte can efficiently suppress the unwanted side reactions by acting on several levels. First, they discourage ion dissolution and formation of intermediate species that typically feed parasitic reactions, including self-decomposition, which is largely reduced thanks to their high chemical stability. The promotion of a denser and more stable SEI induced by RTILs is also desirable to physically screen and protect the electrode surface and thus to block long-term side reactions. The distinct solvent properties of RTILs can also reduce the solubility of by-products into the electrolyte, confining them on the electrode surface.

Provided the mitigated Mn dissolution owing to RTIL-based electrolyte, we need to understand the enhanced structural retention featured by the higher-entropy compounds. The Na–O coordination illustrated in Fig. S7 of SI suggests that $Na^+$ ordering is almost constant among the three compounds across the explored sodiation range. On the other side, the pair distribution functions, *i.e.*, PDFs, for M–O coordination are largely affected by desodiation (see Fig. S8 in SI). Therefore, we dissect the contribution of each metal sublattice to the overall structural evolution upon charge, that is the analysis of distortion modes within any $MO_6$ octahedron. Indeed, $Na^+$ extraction from the layered crystal structure upon cathode charging can induce variations in both cell volume and geometry, potentially affecting phase stability and mechanical integrity. Whether such distortions arise primarily from oxidation of the central M atom or depletion of the Na layer, different metals may exhibit distinct distortion behaviors. The degree of octahedral tilting is evaluated through variations in both M–O bond lengths and O–M–O bond angles within the $MO_6$ octahedron at different sodiation levels. Following the definitions by Nagle-Cocco and Dutton, the variations of bond lengths and bond angles accounting for the octahedral tilting can be quantified in terms of the six VanVleck modes (Q1, …, Q6). By extracting these quantities with the VanVleckCalculator for each M-centered octahedron from our PBE+*U*-D3BJ minimum-energy structures, we could calculate the average distortion magnitude ($\rho$, that contains the information on bond length variations) and the fraction parameter ($\eta$, which relates to the angular motions) as function of desodiation (as shown from the equations displayed on the right-hand side of Fig. 6).[46,47] In LEO (left panels), Ni-based octahedra exhibit increasing $\rho$ values up to $x_{Na} = 0.30$, followed by a sharp decrease at $x_{Na} = 0.12$, while $\eta$ increases steadily upon desodiation (the PDF, reported in Fig. S8, shows significant shifts to lower Ni–O distances with decreasing

 This journal is © The Royal Society of Chemistry 2026

Open Access Article. Published on 09 April 2026. Downloaded on 6/2/2026 11:29:15 AM.
This article is licensed under a Creative Commons Attribution-NonCommercial 3.0 Unported Licence.

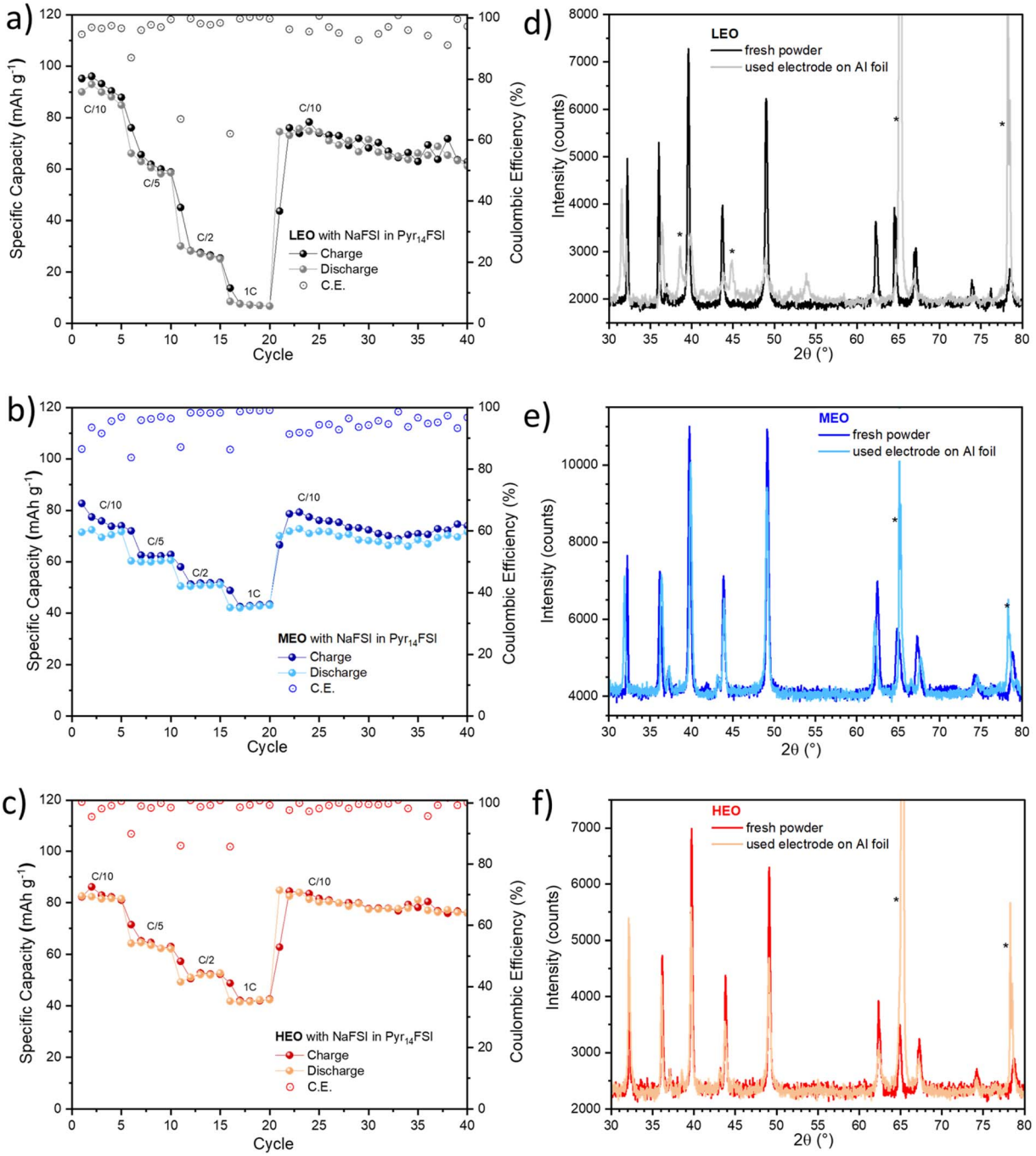


Fig. 5 Specific capacity and coulombic Efficiency of Na-metal cells containing (a) LEO, (b) MEO, and (c) HEO in combination with RTIL-based electrolyte (NaFSI in $Pyr_{14}FSI$ 1 : 4), upon galvanostatic cycling at different C-rates (representative voltage profiles *vs.* specific capacity are reported in Fig. S6). XRD patterns of (d) LEO, (e) MEO, and (f) HEO, comparing the fresh powder and the electrode after galvanostatic cycling with RTIL-based electrolyte (the reflections due to the Al foil current collector are marked with an asterisk).

sodium content, from ~2.05 to ~1.85 Å). The Mn sublattice contributes minimally to the overall distortion (the PDF in Fig. S8 is rather constant upon desodiation, the highest peak lying at ~1.90 Å). In MEO (middle panels), the inclusion of Co, Ti and Mg atoms, yielding a medium-entropy composition, does not significantly alter the octahedral distortions associated with bond lengths (as also mirrored in the PDF of Fig. S8, with the bond length being kept constant in the range 1.8–2.1 Å), but it modifies the angular displacements. Similarly to LEO, Ni-centered octahedra dominate the $\rho$ trend, with negligible contributions from the other metals. However, Mg and Ti markedly impact the fraction parameter, reducing the contribution of shear-type deformations ($\eta << 1$). A similar behavior is observed for HEO (right panels), where Ti-based octahedra limit the angular shear motions and Ni-based ones drive the increasing $\rho$ trend upon charge even after incorporation of Al

Open Access Article. Published on 09 April 2026. Downloaded on 6/2/2026 11:29:15 AM.
This article is licensed under a Creative Commons Attribution-NonCommercial 3.0 Unported Licence.

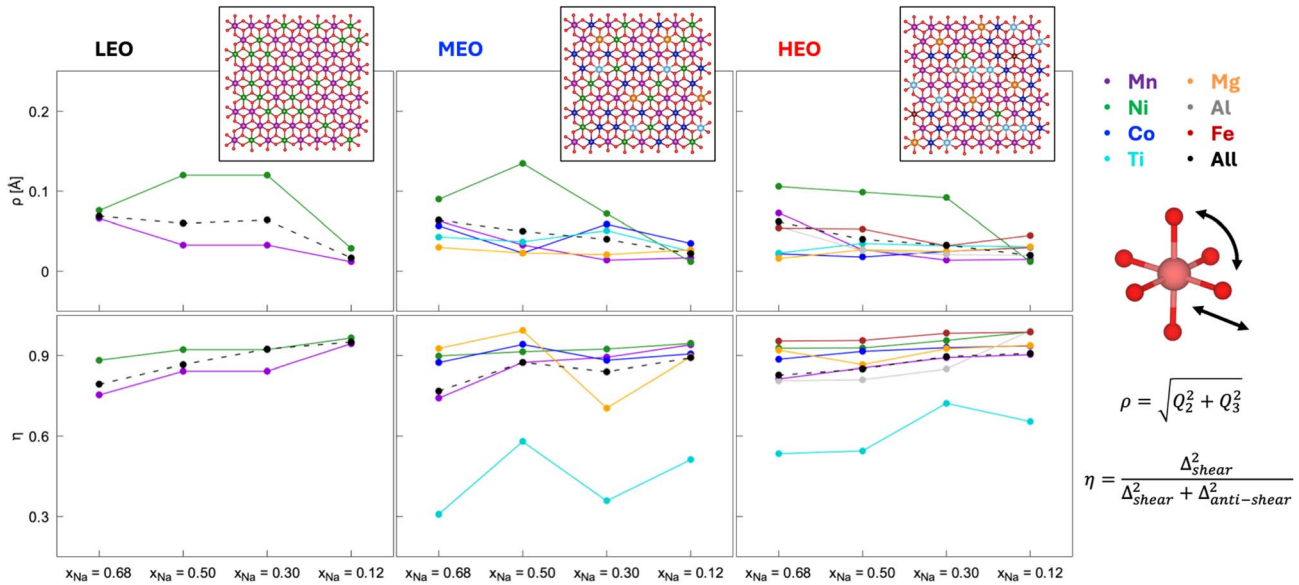


Fig. 6 Structural distortion analysis: magnitude of distortion, $\rho$, and shear fraction parameter, $\eta$, calculated for (from left to right) LEO, MEO, and HEO, with the VanVleckCalculator. Equations are reported on the right side of the figure. Insets: structural detail of the random distribution of metal atoms within the ab lattice plane. Color code: Mn purple, Ni green, Co blue, Ti cyan, Mg orange, Al gray, Fe brown, O red. Atoms are represented as spheres.

and Fe atoms. Because the $\eta$ trend correlates with the angular motion of the oxide ligands, it serves as an indicator of materials' propensity for layer gliding. As demonstrated by Langella *et al.*,[6] the P-to-O phase transition is governed by shear-like deformations; thus, lower $\eta$ values indicate a reduced tendency for phase transformation. Accordingly, increasing configurational entropy seems to enhance cathode phase stability, with MEO and HEO compositions showing lower shear-like structural distortions compared to LEO (see black dashed lines in the three panels). In particular, Ti-centered octahedra play a critical structural role, substantially mitigating distortion effects and promoting structural retention upon desodiation. This analysis aligns well with the XRD patterns of the samples collected before and after the galvanostatic cycling test previously discussed, where HEO and MEO (Fig. 5f and e, respectively) feature a highly retained structure compared to LEO (Fig. 5d).

Also in this case, the functional role of a given metal element appears to be influenced by configurational entropy. For example, the mitigation of shear deformations (reflected by a decrease in $\eta$ values with increasing SoC) ascribed to Ti sublattice is more pronounced in MEO than in HEO. This suggests that the enhanced structural retention in the HEO composition can be ascribed not only to a metal-specific effect, but also to an additional synergic contribution of entropy-driven lattice stabilization.

## 4. Conclusions

In this work, we demonstrated that combining first-principles modeling and electrochemical analysis can lead to a comprehensive knowledge on how configurational entropy governs the behavior of P2-type $Na_xMO_2$ layered oxides cathode materials for Na-ion batteries.

At the purpose, three representative compositions with increasing entropy, *i.e.*, $Na_{0.68}Mn_{0.68}Ni_{0.32}O_2$ (LEO), $Na_{0.68}Mn_{0.44}Ni_{0.19}Co_{0.25}Ti_{0.09}Mg_{0.03}O_2$ (MEO), and $Na_{0.68}Mn_{0.44}Ni_{0.19}Co_{0.19}Ti_{0.09}Mg_{0.03}Al_{0.05}Fe_{0.01}O_2$ (HEO), have been synthesized *via* solid-state reactions and fully characterized by means of XRD measurements, DFT calculations, cyclic voltammetry and galvanostatic cycling in Na-based cells assembled with both standard $NaClO_4$-PC and RTIL-based NaFSI-$Pyr_{14}$FSI electrolytes.

From our outcomes, configurational entropy is shown to be a key driver on several levels.

(i) As unveiled from HSE06-resolved electronic structures and CV profiles, increasing entropy can improve the electrochemical response of the cathode material by enabling charge compensation across multiple redox-active species (*i.e.*, $Co^{3+}/Co^{4+}$ and $Fe^{3+}/Fe^{4+}$ in addition to $Ni^{2+}/Ni^{3+}/Ni^{4+}$), which avoid local over-oxidation, prevent phase transitions (observed instead in the CV of LEO and confirmed by *post-mortem* XRD analysis), reduce voltage hysteresis, thus improving cycling reversibility upon subsequent charging/discharging.

(ii) DFT results on out-of-layer metal migration suggest that increasing entropy can effectively discourage Mn dissolution (*e.g.*, unfavorable formation of $Mn^{2+}/Na_{vac}$ antisite defects), which is instead highlighted as the main cause of cell failure for the low-entropy formulation. While LEO suffers from rapid degradation with conventional carbonate electrolytes, MEO and HEO materials deliver superior cycling stability and capacity retention. In particular, the best performance is obtained by HEO in combination with the RTIL-based NaFSI-$Pyr_{14}$FSI electrolyte (92% of capacity retention at the 40th cycle with respect

 This journal is © The Royal Society of Chemistry 2026

Open Access Article. Published on 09 April 2026. Downloaded on 6/2/2026 11:29:15 AM. This article is licensed under a Creative Commons Attribution-NonCommercial 3.0 Unported Licence.

to the initial capacity of 83 mAh $g^{-1}$), which is consistent with a mitigation of Mn dissolution and with the formation of a dense and stable SEI.

(iii) As evinced from *post-mortem* XRD measurements, increasing entropy can greatly improve structural retention upon cycling. By dissecting each metal contribution to the overall structural evolution upon charge, we elucidate the role of metal mixing in mitigating octahedral distortions occurring upon desodiation and retaining the shear-type deformations that typically drive layer gliding and thus the P-to-O phase transitions.

Overall, configurational entropy emerges as an effective design lever for stabilizing P2-type layered cathodes. This study focuses on a specific set of materials and further efforts would be required to fully assess the transferability of these results, as for example through a systematic exploration of the complete compositional space *via* stepwise elemental incorporation. However, several robust trends already emerge and provide a solid foundation for transferable design guidelines. By implementing broader metal mixing, it is possible to attenuate Jahn–Teller distortions and any octahedral tilting, suppress shear-type lattice deformations linked to P-to-O layer gliding, and distribute charge compensation across multiple redox-active cations. Such collective effects stabilize the host framework and reduce the driving force for detrimental metal ion migration. Beneficial effects are highlighted as metal-specific and may therefore be achieved through appropriate metal doping strategies. For example, Co and Fe act as redox-active elements that promote redox delocalization and stabilize the electronic response, while Ti serves as an electrochemically inert species that suppresses shear-induced structural distortions. However, these mechanisms appear to be further enhanced in the presence of high configurational entropy. Whether exerting direct or indirect effects on the structural and electronic responses to the electrode functioning, mixing entropy engineering can enable robust and durable Na-ion battery performance. These insights provide clear guidelines for the development of next-generation high-entropy layered oxides for sustainable energy storage.

## Author contributions

A. M.: conceptualization, coordination, theoretical modelling and DFT simulations, data analysis and interpretation, manuscript drafting and writing. S. P.: electrochemical measurements, data analysis, figure preparation. M. B.: materials synthesis, conceptualization, coordination, manuscript drafting and writing. A. P.: conceptualization, coordination, electrochemical measurements, data analysis and interpretation, manuscript drafting and writing. H. D.: XRD measurements, data analysis, figure preparation. D. S.: materials synthesis, data analysis and interpretation. G. M.: XRD measurements, data analysis and interpretation. A. B. M. G.: theoretical modelling and DFT simulations, data analysis and interpretation. B. B.: materials synthesis, data analysis and interpretation, manuscript writing. M. P.: theoretical modelling and DFT simulations, data analysis and interpretation, manuscript writing. C. G.: electrochemical measurements, data analysis and interpretation, manuscript writing.

## Conflicts of interest

The authors declare no competing financial interest.

## Data availability

All data supporting the findings of this study are available within the article and its supplementary information (SI). Supplementary information: XRD pattern and Rietveld refinements, lattice parameters obtained from DFT+*U* calculations, theoretical capacity-voltage profile calculated from DFT+*U*, PDOS and average magnetization obtained from hybrid DFT calculations, representative voltage profiles at different C-rate upon galvanostatic charge/discharge cycles, PDF of Na–O and M–O distances. See DOI: https://doi.org/10.1039/d6ta00673f.

## Acknowledgements

The authors acknowledge funding from the ORANGEES project (Italian Ministry of Environment and Energy Security, Research of the National Electric System PTR 2019–2021). The computing resources and the related technical support used for this work have been provided by CRESCO/ENEAGRID High Performance Computing infrastructure and its staff; CRESCO/ENEAGRID High Performance Computing infrastructure is funded by ENEA, the Italian National Agency for New Technologies, Energy and Sustainable Economic Development and by Italian and European research programs. See: https://www.cresco.enea.it/english for information. The EnABLES project received funding from the European Commission under H2020 Research Infrastructures Programme (Grant Agreement 730957). Support under the MUR program "Dipartimenti di Eccellenza 2023–2027" _(CUPE17G22001490006) is gratefully acknowledged.

## References

1 A. Massaro, L. Squillantini, F. D. Giorgio, F. A. Scaramuzzo, M. Pasquali and S. Brutti, Solid-State Sodium-Based Batteries: Advances, Challenges, Perspectives, *Energy*, 2025, **8**, 100357, DOI: 10.1016/j.nxener.2025.100357.

2 K. Kubota, M. Dahbi, T. Hosaka, S. Kumakura and S. Komaba, Towards K-Ion and Na-Ion Batteries as "Beyond Li-Ion.", *Chem. Rec.*, 2018, **18**, 459, DOI: 10.1002/tcr.201700057.

3 M. Ren, H. Fang, C. Wang, H. Li and F. Li, Advances on Manganese-Oxide-Based Cathodes for Na-Ion Batteries | Energy & Fuels, *Energy Fuels*, 2020, **34**(11), 13412, DOI: 10.1021/acs.energyfuels.0c02897.

4 C. Delmas, Sodium and Sodium-Ion Batteries: 50 Years of Research, *Adv. Energy Mater.*, 2018, **8**, 1703137, DOI: 10.1002/aenm.201703137.

5 W. Zuo, A. Innocenti, M. Zarrabeitia, D. Bresser, Y. Yang and S. Passerini, Layered Oxide Cathodes for Sodium-Ion

Open Access Article. Published on 09 April 2026. Downloaded on 6/2/2026 11:29:15 AM. This article is licensed under a Creative Commons Attribution-NonCommercial 3.0 Unported Licence.

Batteries: Storage Mechanism, Electrochemistry, and Techno-Economics, *Acc. Chem. Res.*, 2023, **56**(3), 284–296, DOI: 10.1021/acs.accounts.2c00690.

6 A. Langella, A. Massaro, A. B. Muñoz-García and M. Pavone, Atomistic Insights into Solid-State Phase Transition Mechanisms of P2-Type Layered Mn Oxides for High-Energy Na-Ion Battery Cathodes, *ACS Energy Lett.*, 2025, **10**(3), 1089–1098, DOI: 10.1021/acsenergylett.4c03335.

7 P.-F. Wang, Y. You, Y.-X. Yin and Y.-G. Guo, Layered Oxide Cathodes for Sodium-Ion Batteries: Phase Transition, Air Stability, and Performance, *Adv. Energy Mater.*, 2018, **8**(8), 1701912, DOI: 10.1002/aenm.201701912.

8 A. Langella, A. Massaro, A. B. Muñoz-García and M. Pavone, First-Principles Insights on Solid-State Phase Transitions in P2-$Na_xMnO_2$-Based High Energy Cathode during Na-Ion Battery Operations, *Chem. Mater.*, 2024, **36**(5), 2370–2379, DOI: 10.1021/acs.chemmater.3c02981.

9 X. Li, X. Ma, D. Su, L. Liu, R. Chisnell, S. P. Ong, H. Chen, A. Toumar, J.-C. Idrobo, Y. Lei, J. Bai, F. Wang, J. W. Lynn, Y. S. Lee and G. Ceder, Direct Visualization of the Jahn–Teller Effect Coupled to Na Ordering in $Na_{5/8}MnO_2$, *Nat. Mater.*, 2014, **13**(6), 586–592, DOI: 10.1038/nmat3964.

10 R. J. Clément, P. G. Bruce and C. P. Grey, Review—Manganese-Based P2-Type Transition Metal Oxides as Sodium-Ion Battery Cathode Materials, *J. Electrochem. Soc.*, 2015, **162**(14), A2589, DOI: 10.1149/2.0201514jes.

11 A. Massaro, A. Langella, A. B. Muñoz-García and M. Pavone, First-Principles Insights on Anion Redox Activity in $Na_xFe_{1/8}Ni_{1/8}Mn_{3/4}O_2$: Toward Efficient High-Energy Cathodes for Na-Ion Batteries, *J. Am. Ceram. Soc.*, 2023, **106**(1), 109–119, DOI: 10.1111/jace.18494.

12 A. Massaro, A. Langella, C. Gerbaldi, G. A. Elia, A. B. Muñoz-García and M. Pavone, Ru-Doping of P2-$Na_xMn_{0.75}Ni_{0.25}O_2$-Layered Oxides for High-Energy Na-Ion Battery Cathodes: First-Principles Insights on Activation and Control of Reversible Oxide Redox Chemistry, *ACS Appl. Energy Mater.*, 2022, **5**(9), 10721–10730, DOI: 10.1021/acsaem.2c01455.

13 C.-J. Yu, Y.-C. Pak, C.-H. Kim, J.-S. Kim, K.-C. Ri, K.-H. Ri, S.-H. Choe and S. Cottenier, Structural and Electrochemical Trends in Mixed Manganese Oxides $Na_x(M_{0.44}Mn_{0.56})O_2$ (M = Mn, Fe, Co, Ni) for Sodium-Ion Battery Cathode, *J. Power Sources*, 2021, **511**, 230395, DOI: 10.1016/j.jpowsour.2021.230395.

14 O. Zhanadilov, S. Baiju, N. Voronina, J. H. Yu, A.-Y. Kim, H.-G. Jung, K. Ihm, O. Guillon, P. Kaghazchi and S.-T. Myung, Impact of Transition Metal Layer Vacancy on the Structure and Performance of P2 Type Layered Sodium Cathode Material, *Nano-Micro Lett.*, 2024, **16**(1), 239, DOI: 10.1007/s40820-024-01439-9.

15 J.-W. Yeh, S.-K. Chen, S.-J. Lin, J.-Y. Gan, T.-S. Chin, T.-T. Shun, C.-H. Tsau and S.-Y. Chang, Nanostructured High-Entropy Alloys with Multiple Principal Elements: Novel Alloy Design Concepts and Outcomes, *Adv. Eng. Mater.*, 2004, **6**(5), 299–303, DOI: 10.1002/adem.200300567.

16 J. Wang, S. L. Dreyer, K. Wang, Z. Ding, T. Diemant, G. Karkera, Y. Ma, A. Sarkar, B. Zhou, M. V. Gorbunov, A. Omar, D. Mikhailova, V. Presser, M. Fichtner, H. Hahn, T. Brezesinski, B. Breitung and Q. Wang, P2-Type Layered High-Entropy Oxides as Sodium-Ion Cathode Materials, *Mater. Futur.*, 2022, **1**(3), 035104, DOI: 10.1088/2752-5724/ac8ab9.

17 Y. Ma, Y. Ma, Q. Wang, S. Schweidler, M. Botros, T. Fu, H. Hahn, T. Brezesinski and B. Breitung, High-Entropy Energy Materials: Challenges and New Opportunities, *Energy Environ. Sci.*, 2021, **14**(5), 2883–2905, DOI: 10.1039/D1EE00505G.

18 C. M. Rost, E. Sachet, T. Borman, A. Moballegh, E. C. Dickey, D. Hou, J. L. Jones, S. Curtarolo and J.-P. Maria, Entropy-Stabilized Oxides, *Nat. Commun.*, 2015, **6**(1), 8485, DOI: 10.1038/ncomms9485.

19 A. Sarkar, L. Velasco, D. Wang, Q. Wang, G. Talasila, L. de Biasi, C. Kübel, T. Brezesinski, S. S. Bhattacharya, H. Hahn and B. Breitung, High Entropy Oxides for Reversible Energy Storage, *Nat. Commun.*, 2018, **9**(1), 3400, DOI: 10.1038/s41467-018-05774-5.

20 C. Zhao, F. Ding, Y. Lu, L. Chen and Y.-S. Hu, High-Entropy Layered Oxide Cathodes for Sodium-Ion Batteries, *Angew. Chem., Int. Ed.*, 2020, **59**(1), 264–269, DOI: 10.1002/anie.201912171.

21 A. van de Walle, M. Asta and G. Ceder, The Alloy Theoretic Automated Toolkit: A User Guide, *Calphad*, 2002, **26**(4), 539–553, DOI: 10.1016/S0364-5916(02)80006-2.

22 A. van de Walle, R. Sun, Q.-J. Hong and S. Kadkhodaei, Software Tools for High-Throughput CALPHAD from First-Principles Data, *Calphad*, 2017, **58**, 70–81, DOI: 10.1016/j.calphad.2017.05.005.

23 G. Kresse, Efficient Iterative Schemes for *Ab Initio* Total-Energy Calculations Using a Plane-Wave Basis Set, *Phys. Rev. B: Condens. Matter Mater. Phys.*, 1996, **54**(16), 11169–11186, DOI: 10.1103/PhysRevB.54.11169.

24 P. E. Blöchl, Projector Augmented-Wave Method, *Phys. Rev. B*, 1994, **50**(24), 17953–17979, DOI: 10.1103/PhysRevB.50.17953.

25 G. Kresse, From Ultrasoft Pseudopotentials to the Projector Augmented-Wave Method, *Phys. Rev. B: Condens. Matter Mater. Phys.*, 1999, **59**(3), 1758–1775, DOI: 10.1103/PhysRevB.59.1758.

26 A. Massaro, A. B. Muñoz-García, P. P. Prosini, C. Gerbaldi and M. Pavone, Unveiling Oxygen Redox Activity in P2-Type $Na_xNi_{0.25}Mn_{0.68}O_2$ High-Energy Cathode for Na-Ion Batteries, *ACS Energy Lett.*, 2021, **6**(7), 2470–2480, DOI: 10.1021/acsenergylett.1c01020.

27 J. P. Perdew, Generalized Gradient Approximation Made Simple, *Phys. Rev. Lett.*, 1996, **77**(18), 3865–3868, DOI: 10.1103/PhysRevLett.77.3865.

28 V. I. Anisimov, Band Theory and Mott Insulators: Hubbard *U* Instead of Stoner I, *Phys. Rev. B: Condens. Matter Mater. Phys.*, 1991, **44**(3), 943–954, DOI: 10.1103/PhysRevB.44.943.

29 S. Grimme, J. Antony, S. Ehrlich and H. Krieg, A Consistent and Accurate *Ab Initio* Parametrization of Density Functional Dispersion Correction (DFT-D) for the 94 Elements H-Pu, *J. Chem. Phys.*, 2010, **132**(15), 154104, DOI: 10.1063/1.3382344.

30 J. Heyd and G. E. Scuseria, Efficient Hybrid Density Functional Calculations in Solids: Assessment of the

 This journal is © The Royal Society of Chemistry 2026

Open Access Article. Published on 09 April 2026. Downloaded on 6/2/2026 11:29:15 AM. This article is licensed under a Creative Commons Attribution-NonCommercial 3.0 Unported Licence.

Heyd–Scuseria–Ernzerhof Screened Coulomb Hybrid Functional, *J. Chem. Phys.*, 2004, **121**(3), 1187–1192, DOI: 10.1063/1.1760074.

31 J. Wang, S. L. Dreyer, K. Wang, Z. Ding, T. Diemant, G. Karkera, Y. Ma, A. Sarkar, B. Zhou, M. V. Gorbunov, A. Omar, D. Mikhailova, V. Presser, M. Fichtner, H. Hahn, T. Brezesinski, B. Breitung and Q. Wang, P2-Type Layered High-Entropy Oxides as Sodium-Ion Cathode Materials, *Mater. Futur.*, 2022, **1**(3), 035104, DOI: 10.1088/2752-5724/ac8ab9.

32 G. Wan, B. Peng, L. Zhao, F. Wang, L. Yu, R. Liu and G. Zhang, *Dual-strategy Modification on P2-$Na_{0.67}Ni_{0.33}Mn_{0.67}O_2$ Realizes Stable High-voltage Cathode and High Energy Density Full Cell for Sodium-ion Batteries, SusMat*, 2023, **3**, 58, DOI: 10.1002/sus2.105.

33 C. Ke, F. Fu, J. Zheng and W. Yang, P2-$Na_{2/3}Mn_{0.66}Ni_{0.21}Mg_{0.05}Al_{0.03}X_{0.0225}O_2$ (X = Zr, Ce) as High-Performance Cathode Materials for Sodium-Ion Batteries, *Ionics*, 2020, **26**(2), 727–734, DOI: 10.1007/s11581-019-03216-w.

34 A. Zunger, Special Quasirandom Structures, *Phys. Rev. Lett.*, 1990, **65**(3), 353–356, DOI: 10.1103/PhysRevLett.65.353.

35 M. Islam, M. Akbar, D. Han, B. Ali, Y. Jeong Choi, J. Lee, G. Choi, J.-H. Park, J.-Y. Kim, H.-G. Jung, K. Yoon Chung, D. Kim, Y.-M. Kang and K.-W. Nam, Unraveling Vacancy-Induced Oxygen Redox Reaction and Structural Stability in Na-Based Layered Oxides, *Chem.–Eng. J.*, 2022, **431**, 133962, DOI: 10.1016/j.cej.2021.133962.

36 K. Xue, S. Yang, F. Lai, X. Zhang, Y. Xie, G. Yang, K. Pan, Q. Li and H. Wang, Synergistic Effect of Anchoring Transitional/Interstitial Sites on Boosting Structural and Electrochemical Stability of O3-Type Layered Sodium Oxides, *ACS Appl. Mater. Interfaces*, 2025, **17**(1), 1286–1294, DOI: 10.1021/acsami.4c17755.

37 M. Yan, Z.-A. Jin, P. Wang, Y. Guo, Y.-X. Yin and S. Xu, In Situ Surface Engineering O3-Layered Oxide Cathode *via* $Na_3PO_4$/P3-Layered Oxide Dual Coating Layers, *Electrochim. Acta*, 2025, **521**, 145911, DOI: 10.1016/j.electacta.2025.145911.

38 K. Hemalatha, M. Jayakumar and A. S. Prakash, Influence of the Manganese and Cobalt Content on the Electrochemical Performance of P2-$Na_{0.67}Mn_xCo_{1-x}O_2$ Cathodes for Sodium-Ion Batteries, *Dalton Trans.*, 2018, **47**(4), 1223–1232, DOI: 10.1039/C7DT04372D.

39 A. Bhandari and J. Bhattacharya, Review—Manganese Dissolution from Spinel Cathode: Few Unanswered Questions, *J. Electrochem. Soc.*, 2016, **164**(2), A106, DOI: 10.1149/2.0101614jes.

40 S. Guo, Y. Sun, P. Liu, J. Yi, P. He, X. Zhang, Y. Zhu, R. Senga, K. Suenaga, M. Chen and H. Zhou, Cation-Mixing Stabilized Layered Oxide Cathodes for Sodium-Ion Batteries, *Sci. Bull.*, 2018, **63**(6), 376–384, DOI: 10.1016/j.scib.2018.02.012.

41 Z.-C. Jian, J.-X. Guo, Y.-F. Liu, Y.-F. Zhu, J. Wang and Y. Xiao, Cation Migration in Layered Oxide Cathodes for Sodium-Ion Batteries: Fundamental Failure Mechanisms and Practical Modulation Strategies, *Chem. Sci.*, 2024, **15**(47), 19698–19728, DOI: 10.1039/D4SC05206D.

42 K. Kubota, T. Asari and S. Komaba, Impact of Ti and Zn Dual-Substitution in P2 Type $Na_{2/3}Ni_{1/3}Mn_{2/3}O_2$ on Ni–Mn and Na-Vacancy Ordering and Electrochemical Properties, *Adv. Mater.*, 2023, **35**(26), 2300714, DOI: 10.1002/adma.202300714.

43 L. G. Chagas, S. Jeong, I. Hasa and S. Passerini, Ionic Liquid-Based Electrolytes for Sodium-Ion Batteries: Tuning Properties To Enhance the Electrochemical Performance of Manganese-Based Layered Oxide Cathode, *ACS Appl. Mater. Interfaces*, 2019, **11**(25), 22278–22289, DOI: 10.1021/acsami.9b03813.

44 C. Wang, L. Xing, J. Vatamanu, Z. Chen, G. Lan, W. Li and K. Xu, Overlooked Electrolyte Destabilization by Manganese (II) in Lithium-Ion Batteries | Nature Communications, *Nat. Commun.*, 2019, **10**, 3423, DOI: 10.1038/s41467-019-11439-8.

45 H. Liu, X. Gao, J. Chen, J. Gao, S. Yin, S. Zhang, L. Yang, S. Fang, Y. Mei, X. Xiao, L. Chen, W. Deng, F. Li, G. Zou, H. Hou and X. Ji, Reversible OP4 Phase in P2–$Na_{2/3}Ni_{1/3}Mn_{2/3}O_2$ Sodium Ion Cathode, *J. Power Sources*, 2021, **508**, 230324, DOI: 10.1016/j.jpowsour.2021.230324.

46 J. H. Van Vleck, The Jahn-Teller Effect and Crystalline Stark Splitting for Clusters of the Form XY6, *J. Chem. Phys.*, 1939, **7**, 72, DOI: 10.1063/1.1750327.

47 L. a. V. Nagle-Cocco and S. E. Dutton, Van Vleck Analysis of Angularly Distorted Octahedra Using VanVleckCalculator, *J. Appl. Crystallogr.*, 2024, **57**(1), 20–33, DOI: 10.1107/S1600576723009925.